communications engineering

A Nature Portfolio journal

Article

https://doi.org/10.1038/s44172-025-00534-y

Democratizing high-Q plasmonic optical fiber biosensing with low-resolution interrogation and Fourier demodulation

Hadrien Fasseaux [1] ✉, Médéric Loyez [1,2] & Christophe Caucheteur[1]

Gold-coated tilted fiber Bragg gratings have established themselves as powerful plasmonic biosensors, but their widespread deployment remains hindered by the need for costly, high-resolution interrogators and complex signal processing. Here, we demonstrate that tilted fiber Bragg gratings sensors can be effectively interrogated using a low-cost, coarsely resolved fiber Bragg grating interrogator with only 256 pixels spanning 45 nm, corresponding to a low resolution (~180 pm, 10 times coarser than standard interrogators). By applying a fast Fourier transform-based demodulation technique to the dense, comb-like cladding mode spectrum, we extract robust sensing information using only a narrow spectral window of a few tens of nanometers. This dramatically reduces hardware and computational requirements while preserving high sensitivity. We validate our approach in both refractometry and biosensing, targeting the clinically relevant biomarker Proteinase 3. Furthermore, we show that temperature cross-sensitivity can be compensated directly within this narrow spectral range by tracking a dedicated cladding mode resonance, eliminating the need to reference the Bragg mode. These advances pave the way for compact, cost-effective, and user-friendly plasmonic fiber sensor systems deployable in real-world biomedical environments.

Over the past two decades, tilted fiber Bragg gratings (TFBGs) have emerged as a cornerstone technology in optical biosensing, particularly when coated with a nanometric gold film to excite surface plasmon resonances (SPRs). These plasmonic TFBGs uniquely combine the high surface sensitivity of SPRs with the inherent advantages of optical fibers, including compactness, easy light injection, immunity to electromagnetic interference, and in situ operation with remote interrogation[1–6]. Their rich spectral signature, composed of dozens of narrow cladding mode resonances spanning a broad wavelength range, provides an information-dense platform for highly sensitive detection of refractive index (RI) changes and biomolecular interactions at their outer surface[7–10].

Among the various classes of plasmonic optical fiber biosensors, gold-coated tilted fiber Bragg gratings (SPR-TFBGs) have consistently demonstrated superior sensing performance, owing to their combination of high refractive index sensitivity and narrow, well-defined resonance features. This combination enhances both detection limit and noise resilience, making TFBGs a compelling platform for label-free biosensing. Unlike etched or U-bent multimode optical fibers or long period fiber gratings[11,12], which typically excite a broad, low-Q plasmonic band, TFBGs produce ultra-narrow spectral features (often below 0.2 nm full width at half maximum) with high signal-to-noise ratios and polarization dependence. As a result, the ratio between the RI sensitivity and the spectral linewidth of the resonance exceeding several hundreds to over a thousand RIU^{-1} have been reported[10], outperforming competing architectures by an order of magnitude. Moreover, the distributed comb-like spectrum of TFBGs allows for multi-mode tracking[13], further enhancing stability, resolution, and robustness against noise. This makes TFBGs particularly well suited for applications requiring ultra-low detection limits, such as biomarker diagnostics, environmental sensing, and lab-on-fiber systems.

Because of this high-Q nature, the interrogation of gold-coated TFBGs has relied on high-resolution, and often expensive, optical spectrum analyzers or finely-resolved interrogators. In most reported works, a single cladding mode resonance is tracked, either in wavelength shift or amplitude modulation, to infer local changes in the surrounding medium. While this technique remains widely adopted, its practical implementation is often limited by system complexity, cost, and robustness issues in real-world settings. The need for high-resolution equipment also imposes constraints on the miniaturization and portability of TFBG-based biosensing systems, hampering their broader adoption in clinical, environmental, and industrial applications.

[1]Département d'électromagnétisme et télécommunications, Institut des Matériaux, UMons, Mons, Belgium. [2]Département de Protéomique et de Microbiologie, UMons, Mons, Belgium. ✉e-mail: Hadrien.fasseaux@umons.ac.be

In this work, we introduce a paradigm shift in the demodulation of plasmonic TFBG sensors by demonstrating that a coarsely resolved fiber Bragg grating interrogator featuring a modest close to 180 pm wavelength resolution can be leveraged to extract relevant sensing information with high fidelity. The key to this breakthrough lies in its combination with a powerful demodulation method based on the fast Fourier transform (FFT) of the transmitted spectrum. This approach effectively harnesses the spectral density of cladding mode resonances and transforms their complex comb-like structure into a highly informative frequency-domain signature. Not only does this simplify the analysis pipeline, but it also substantially reduces hardware requirements, offering a cost-effective and user-friendly alternative to conventional techniques.

We demonstrate the effectiveness of this method in both refractometric and biosensing scenarios. Remarkably, we show that only a narrow spectral window spanning a few tens of nanometers is sufficient for reliable sensing, drastically reducing data acquisition and processing overheads. Additionally, we provide experimental evidence that temperature compensation, a critical challenge in biosensing, can be achieved using a dedicated cladding mode resonance rather than relying on the Bragg mode. This further enhances the practicality of the approach, eliminating the need for additional reference gratings or environmental isolation strategies.

By addressing key limitations in interrogator cost, spectral bandwidth, and temperature cross-sensitivity, this work paves the way for broader deployment of TFBG biosensors in portable and field-deployable platforms. It represents a significant advance in the transition of plasmonic fiber sensing from lab-scale research to scalable, real-world applications.

Results

General spectral characteristics

An SPR-TFBG is a sensor in which a Bragg grating is inscribed within the core of a single-mode optical fiber with a tilt relative to the fiber cross-section, as illustrated in Fig. 1a. This angular configuration enables efficient coupling between the guided core mode and a series of cladding modes, giving rise to distinct resonances observable in the transmission amplitude spectrum (Fig. 1b), as measured by an optical spectrum analyzer. The resulting resonance features, spaced ~1 nm to 1.5 nm apart, correspond to modal interference patterns, including the self-coupled Bragg resonance at the right end of the spectrum. To facilitate surface plasmon excitation and thereby increase RI sensitivity, the fiber's cladding is coated with a thin gold film, typically around 50 nm thick. A characteristic spectral constriction, whose position depends on the SRI, signals the excitation of a surface plasmon at the metal-surrounding dielectric interface.

Traditional interrogation techniques rely on direct spectral analysis; monitoring resonance shifts or amplitude variations[14]. However, recent advances in signal processing have introduced alternative strategies to improve sensing accuracy and robustness. One such method applies Fourier transform filtering techniques to convert this spectral comb into a spectrum exhibiting a single resonance, the SPR[15,16]. Specifically, after applying a FFT to the IL spectrum, the spatial frequency decomposition reveals three doublets corresponding to the first, second, and third harmonics (Fig. 1c). By isolating the first harmonic using a fourth-order Gaussian filter and applying an inverse Fourier transform to the result, one obtains a curve with a local minimum located at the resonance wavelength (Fig. 1d). This spectral simplification enables straightforward minimum tracking of the SPR shift, which exhibits a quasi-linear evolution with the RI. Importantly, this is achieved without relying on any interpolation between spectra.

Figure 1e presents the evolution of this filtered signal in three dimensions as the SRI increases. The dark green curve denotes the spectrum at the initial RI, while the red trajectory highlights the progression of the minimum across the RI range. The projection onto the wavelength-SRI plane (Fig. 1f) highlights the linear correlation between the minimum's position and the SRI. This Fourier-domain filtering approach offers a robust, interpolation-free demodulation strategy that enhances linearity and sensitivity while reducing computational complexity.

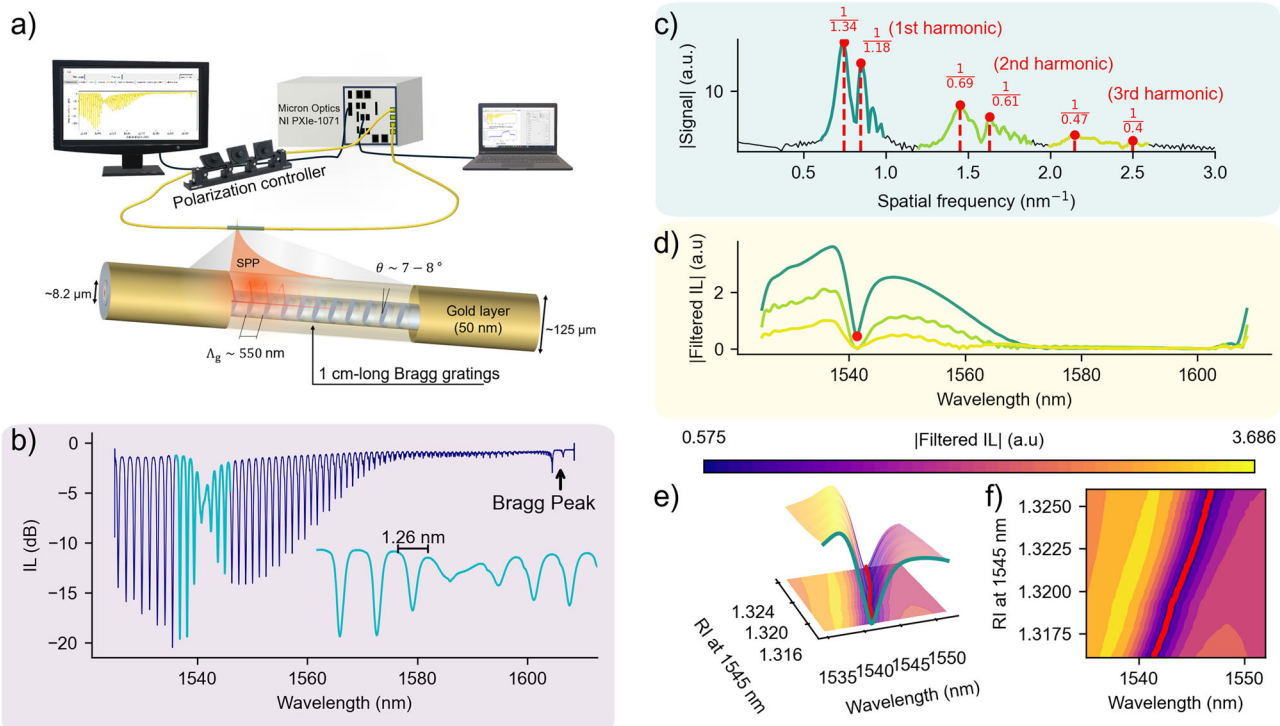

Fig. 1 | Fourier-based analysis of the gold-coated tilted fiber Bragg grating (SPR-TFBG) response. a Schematic representation of the interrogation setup for SPR-TFBG. **b** Experimental insertion loss (IL) spectrum of the transverse magnetic polarized mode for an SPR-TFBG immersed in water. **c** Positive-frequency component of the Fourier-transformed IL spectrum. **d** Filtered IL spectrum for each harmonic, with the red marker indicating the tracked spectral position. **e** Three-dimensional representation of the first harmonic's filtered spectrum (experimental data) as a function of surrounding refractive index (RI). **f** Projection of (**e**) onto the wavelength-RI plane.

Temperature compensation

While SPR-TFBGs are commonly employed to monitor changes in the SRI, the presence of the Bragg resonance, analogous to that in standard FBGs, enables simultaneous temperature tracking and compensation. This feature is particularly valuable when thermal effects impact RI measurements, which represents the vast majority of practical cases. Indeed, temperature variations induce changes in the RI of water, following[17]

$$n(\lambda, T) = A(T) + \frac{B(T)}{\lambda^2} + \frac{C(T)}{\lambda^4} + \frac{D(T)}{\lambda^6}, \tag{1}$$

where the temperature-dependent coefficients $A(T)$, $B(T)$, $C(T)$, and $D(T)$ are defined as follows[17]:

$$A(T) = 1.3208 - 1.2325 \times 10^{-6} T - 1.8674 \times 10^{-6} T^2 + 5.0233 \times 10^{-9} T^3, \tag{2}$$

$$B(T) = 5208.2413 - 0.5179 T - 2.284 \times 10^{-2} T^2 + 6.9608 \times 10^{-5} T^3 nm^2, \tag{3}$$

$$C(T) = -2.5551 \times 10^{8} - 18341.336 T - 917.2319 T^2 + 2.7729 T^3 nm^4, \tag{4}$$

$$D(T) = 9.3495 + 1.7855 \times 10^{-3} T + 3.6733 \times 10^{-5} T^2 - 1.2932 \times 10^{-7} T^3 nm^6. \tag{5}$$

Thus, in the experiments reported herafater, we conducted all measurements in pure water under passive cooling, rather than using solutions with varying RIs. Before analyzing RI-induced variations, we first bring the confirmation that the Bragg resonance in a TFBG behaves similarly to that of a conventional FBG. To characterize its thermal sensitivity, we immersed an SPR-TFBG and a co-located reference FBG in pure water initially at ~ 50 °C, and allowed the system to cool passively to ambient temperature. As illustrated in Fig. 2a, spectra were acquired concurrently using a high-resolution interrogator and a lower-resolution device (see sections Interrogation device and Experimental setup for temperature and RI characterization). The corresponding spectra are shown in Fig. 2b, c, with insets displaying the Bragg peaks fitted using a Voigt function. This fitting allows precise localization of the Bragg wavelength, marked by vertical lines at the maxima of the fitted profiles.

The Voigt function, defined as the convolution of a Gaussian and a Lorentzian profile, offers improved accuracy over a purely Gaussian model, particularly in the presence of asymmetries. Figure 2d displays the evolution of the Bragg peak positions throughout the cooling ramp. Two main observations emerge: (i) both the SPR-TFBG and the reference FBG exhibit comparable thermal responses, confirming the use of the Bragg feature as a reliable temperature probe; and (ii) the sensitivity measured using the low-resolution system is ~15% lower.

Moreover, when the Bragg resonance lies outside the interrogation window due to spectral range limitations, temperature compensation may still be achieved by monitoring alternative spectral features.

Figure 2e shows a magnified view of the high-resolution SPR-TFBG spectrum, with 30 labeled resonances, five of which are highlighted. As shown in Fig. 2f, which presents a 3D view of the evolution of $\Delta\lambda_i$ over time during passive cooling, all peaks exhibit a blueshift as the temperature decreases, although the extent of the shift varies. Modes showing the largest downward shift, such as $i = 1$ and $i = 30$, are predominantly driven by temperature changes and are located at the spectral edges. These modes are minimally affected by refractive index variations of the surrounding medium, making them suitable references for temperature compensation. In contrast, modes located near the SPR attenuation band, such as $i = 8$, are subject to both thermal and refractive index effects, with the RI variation acting in opposition to the thermally induced blueshift, thus effectively slowing their spectral evolution. The black vertical lines in Fig. 2f indicate the final $\Delta\lambda_i$ for the five highlighted peaks ($i = 1$, $i = 8$, $i = 16$, $i = 20$, and $i = 30$). The Fig. 2f also shows the evolution of the Bragg peak, which is insensitive to RI changes and therefore exhibits the largest absolute $\Delta\lambda_i$ shift, amounting to -0.248 nm over the experiment. Among the cladding modes, the largest shifts were observed for $i = 1$ (-0.221 nm) and $i = 30$ (-0.216 nm), closely matching the Bragg peak shift. Modes $i = 8$, $i = 16$, and $i = 20$ showed smaller shifts of -0.151 nm, -0.209 nm, and -0.187 nm, respectively. Although the peak at $i = 16$ appears weakly sensitive to RI changes, in cases where the Bragg peak is inaccessible, temperature compensation is best performed by aligning the spectra on cladding modes with low effective RIs, such as $i = 1$, corresponding to modes radiated in a bare TFBG.

Refractive index tracking

As indicated by Eq. (1), variations in the RI arise from temperature changes that affect all features of the ILs. As discussed in the general spectral characteristics section, the method used to extract RI variations relies on filtering in the Fourier domain. We first examine the effect of reduced spectral resolution on the filtered spectrum.

Spectral resolution effect. In theory[18], the SPR wavelength is given by:

$$\lambda^{\mathrm{SPR}} = \left(n_{\mathrm{eff}}^{\mathrm{co}} + \sqrt{\frac{\varepsilon_m \varepsilon_d}{\varepsilon_m + \varepsilon_d}} \right) \frac{\Lambda}{\cos\theta}, \tag{6}$$

where $\varepsilon_d = n^2$ denotes the dielectric permittivity of water, $n_{\mathrm{eff}}^{\mathrm{co}} = 1.447$ represents the effective refractive index of the core mode, ε_m denotes the permittivity of gold, and $\Lambda/\cos\theta$ specifies the projection of the grating period onto the fiber axis, with θ being the tilt angle of the grating relative to the fiber cross-sectional plane.

This enables extraction of the SPR wavelength, λ^{SPR}, indicated by the red and blue markers in Fig. 3a presenting the results of the filtering-based method applied to spectra recorded during the cooling experiment from both interrogation systems. To enhance the precision of the SPR wavelength determination in addition to the approach developed in the general spectral characteristics section, we introduced zero-padding in the Fourier domain after filtering. While this operation does not add spectral information, it increases the sampling resolution to 0.1 pm, thereby improving the localization of the SPR minimum without requiring curve fitting. Figure 3a shows consistent identification of the SPR dip despite differing native spectral resolutions. The temporal evolution of λ^{SPR} is shown in the lower panel of Fig. 3b. While both systems exhibit similar trends, the lower-resolution instrument underestimates the SPR shift during cooling, with a maximum deviation of approximately 12% relative to the shift measured by the high-resolution system. This discrepancy is quantified in the upper panel of Fig. 3b, which plots the temporal residual error, defined as:

$$\Delta\lambda_{\Delta\mathrm{inst.}}^{\mathrm{SPR}} = \frac{\lambda_{180\,\mathrm{pm}}^{\mathrm{SPR}} - \lambda_{4\,\mathrm{pm}}^{\mathrm{SPR}}}{\lambda_{4\,\mathrm{pm}}^{\mathrm{SPR}}}. \tag{7}$$

Additionally, we demonstrate that the analysis method reliably retrieves the SPR wavelength. By combining Eq. (1) and Eq. (6), and using the gold permittivity values from Yakubovsky et al.[19], we computed the semi-theoretical evolution $\lambda_{\mathrm{SPR}}^{\mathrm{th}}(T)$. The grating period was experimentally estimated from the Bragg wavelength:

$$\lambda_B = 2 n_{\mathrm{eff}}^{\mathrm{co}} \frac{\Lambda}{\cos\theta}. \tag{8}$$

As shown in Fig. 3c, the experimental values of λ^{SPR} diverge from the theoretical curve due to temperature-induced RI changes. However, once temperature is compensated for, either via the Bragg peak shift or a cladding mode located on the low-wavelength side of the SPR dip, the experimental results closely match the theoretical model. This underscores both the importance of temperature compensation in non-isothermal sensing

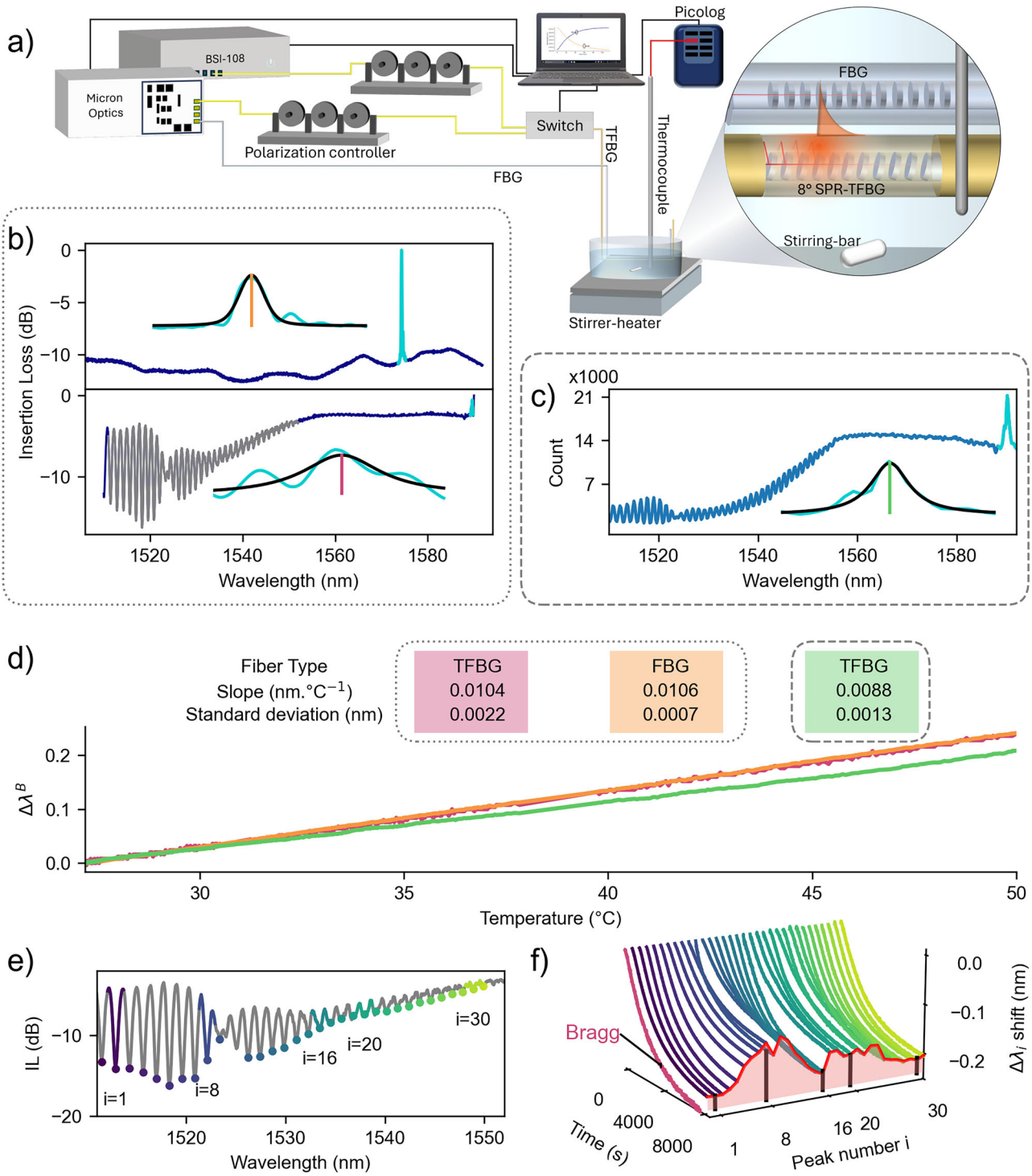

Fig. 2 | Spectral characterization and temperature tracking of a gold-coated tilted fiber Bragg grating (SPR-TFBG) during passive cooling. a Experimental setup for monitoring spectral shifts in an SPR-TFBG and a reference fiber Bragg grating (FBG) immersed in water at ~50 °C. **b** High-resolution insertion loss (IL) spectra. Top panel: Reference FBG, total IL in purple, Bragg peak in turquoise. Inset: zoom on Bragg peak with Voigt fit (black) and maximum indicated by vertical orange line. Bottom panel: Gold-coated SPR-TFBG, total IL in purple, Bragg peak in turquoise, region corresponding to (**e**) in gray. Inset: zoom on Bragg peak with Voigt fit (black) and maximum indicated by vertical red-pink line. **c** SPR-TFBG spectrum acquired with BSI-108 interrogator. Total IL in blue, Bragg peak in turquoise. Inset: zoom on Bragg peak with Voigt fit (black) and maximum indicated by vertical green line. **d** Evolution of Bragg wavelength from Voigt fits. **e** Zoom on SPR-TFBG spectrum shown in (**b**). **f** 3D view of $\Delta\lambda_i$ for all 30 peaks during passive cooling. Vertical black lines mark the five peaks highlighted in (**e**).

environments and the potential of cladding modes as effective temperature references.

Interrogation range effect. To evaluate the influence of the interrogated wavelength range, we repeated the experiment using a BSI-104 interrogator, which offers a narrower spectral window compared to the BSI-108 (see interrogation device section). An SPR-TFBG with a tilt angle of 8° was selected to ensure that the SPR dip remained within the accessible spectral range. However, under this configuration, the Bragg peak falls outside the interrogation window. Figure 4a, e displays the

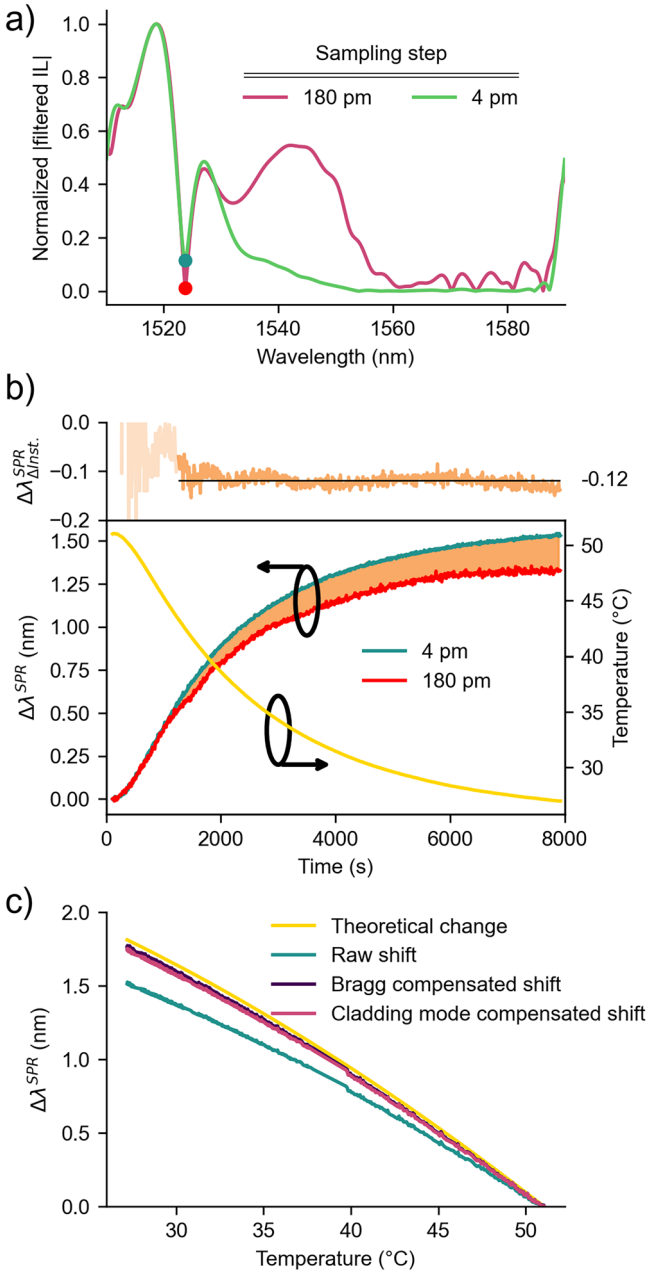

Fig. 3 | Resolution dependency of surface plasmon resonance (SPR) wavelength shift and temperature compensation. a Filtered insertion loss (IL) spectrum of a gold-coated tilted fiber Bragg grating (SPR-TFBG) showing the extraction of the resonance minimum for both interrogation systems: MicronOptics and BSI-108 with 4 pm and 180 pm of sampling step respectively. **b** Temporal evolution of the SPR wavelength extracted, compared to the temperature measured by a thermocouple. The upper part shows the temporal residual deviation between low and high-resolution interrogators. **c** Comparison between the experimental and theoretical evolution of the SPR wavelength, computed using temperature-dependent refractive index models.

spectra recorded with the BSI-108 and BSI-104, respectively. In Fig. 4a, the orange-shaded area delineates the spectral subset covered by the BSI-104.

As shown in Fig. 4b, filtering the spectrum within either the full or truncated window yields the same resonance position, and Fig. 4c further confirms that the dependence of the SPR wavelength on the refractive index is preserved.

Figure 4d investigates the robustness of SPR wavelength detection as the spectral window is progressively narrowed. The extracted wavelength remains stable as long as an interrogated range of ~25 nm is retained around the SPR feature. Below this threshold, edge effects introduce distortions that may shift the apparent minimum and reduce accuracy.

Measurements acquired with the BSI-104 support these observations. Figure 4f, c presents the filtered spectra and the corresponding temperature evolution, demonstrating that SPR-based sensing remains robust under moderate spectral truncation, provided the attenuation dip is sufficiently captured.

Biosensing application

As previously noted, SPR-TFBGs can serve as biosensors following functionalization with receptors specific to the target analyte[20]. Using the setup shown in Fig. 5a, we simultaneously tracked the evolution of the filtered spectrum minimum during biofunctionalization and biodetection steps with two instruments of differing resolution (MicronOptics and BSI-108). The analyte consisted of proteinase 3 (PR3) antigens (C-ANCA), purified from human neutrophils. As in our previous work[15], the SPR-TFBG sensor was placed within a microfluidic chamber connected to a control flow and solution system.

Figure 5b shows the surface functionalization results. Each solution induces a clear, distinct spectral shift in both instruments. Notably, the sensitivity measured with the BSI-108 is ~13% lower than with the MicronOptics system (upper panel, Fig. 5b) as it was expected from the spectral resolution effect section. This reduction does not impair detection of autoantibodies in patient serum. Due to the absence of international standards in autoimmunity, precise quantification of autoantibody levels was not possible; serum dilutions followed supplier guidelines.

While absolute spectral shifts cannot be used as a direct diagnostic metric, the relative change in signal before and after serum exposure, followed by rinsing, provides a robust detection criterion. Spectral responses from control (top) and positive (bottom) serum samples are shown in Fig. 5c. To assess detectability, we define a positive result as a relative shift exceeding three times the standard deviation (σ) of the baseline signal, calculated from the sensor response while immersed in buffer prior to analyte exposure.

Error bars in Fig. 5d represent $\pm 1.96\sigma$ for each trace. The factor 1.96 corresponds to the 95% confidence interval assuming a normal distribution of baseline fluctuations. Each trace corresponds to a single measurement per instrument and condition; thus, the error bars reflect the intrinsic variability of the sensor signal under the experimental conditions, providing a realistic estimate of the measurement uncertainty in the absence of standardized reference materials for autoantibody quantification. As illustrated, only the positive sample crosses this 3σ threshold, while the control remains well below it, confirming reliable discrimination between the two conditions without requiring absolute calibration.

This binary approach is consistent with clinical practice, where ANCA serology is typically used to confirm or exclude a suspected diagnosis rather than to quantify antibody concentration. The most common methods include ELISA, with a positivity threshold defined at 20 U/mL, and indirect immunofluorescence (IIF), where titers above 1:8 are considered positive[21–24]. In our case, the supplier confirmed that the serum samples were pre-characterized as either positive or negative. No numerical thresholds were provided, and the results are interpreted qualitatively. Consequently, the comparison shown in Fig. 5d relies on juxtaposing the two conditions to highlight differential spectral responses. Moreover, precise quantification using a limit of detection would only be meaningful if accurate threshold values could be defined. This is not compatible with the post-diagnostic clinical context described above, where serological results support or refute an already established clinical suspicion.

Discussion

This work establishes a new methodological pathway for the interrogation of high-Q plasmonic TFBG sensors, leveraging their dense spectral response through a compact, low-resolution readout strategy. Building upon the approach introduced in our previous work[14], we enhance its applicability by

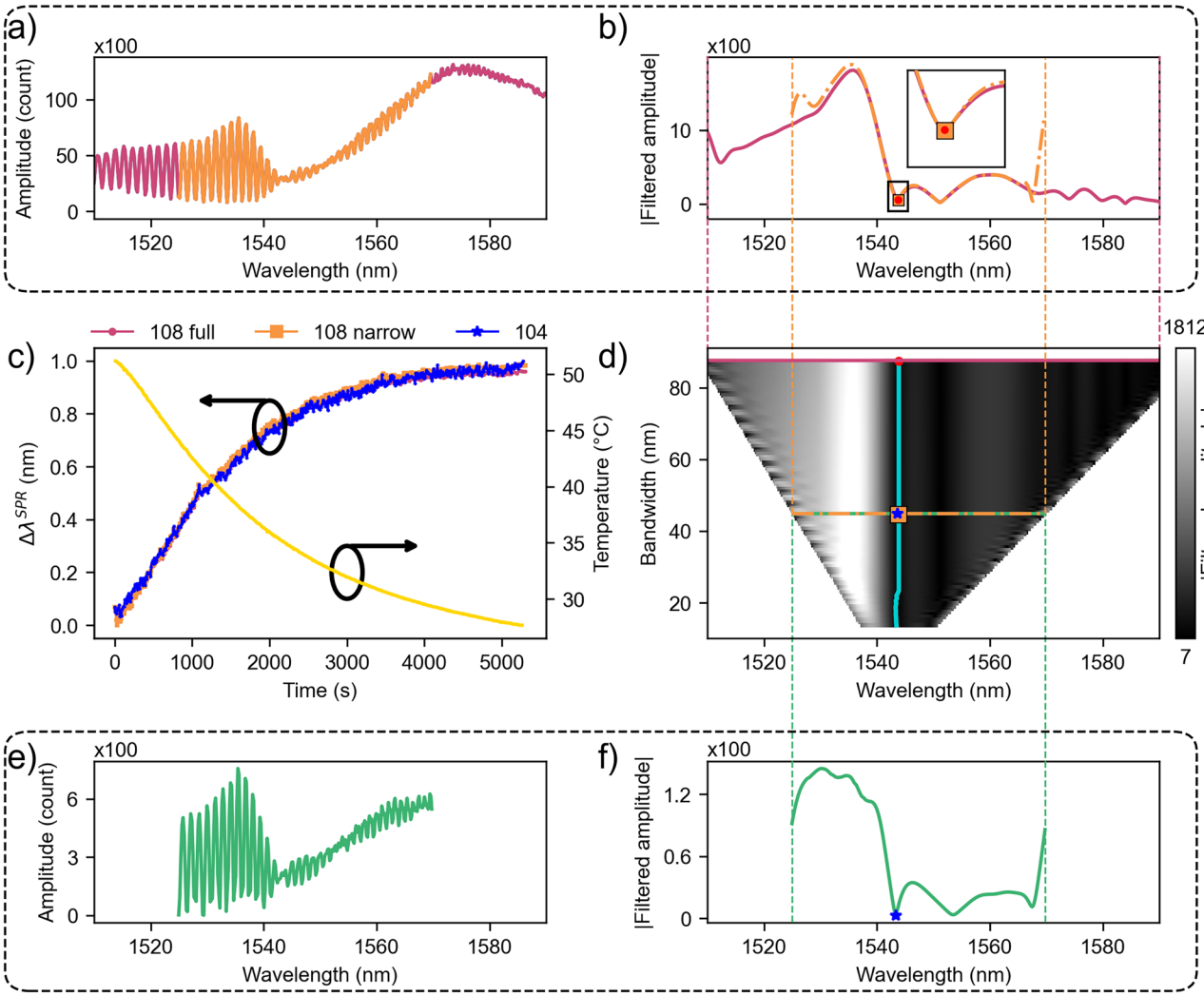

Fig. 4 | Robustness of surface plasmon resonance (SPR) tracking under spectral range limitations. a Insertion loss spectrum of an 8° gold-coated tilted fiber Bragg grating (SPR-TFBG) interrogated with the wide-range interrogator (BSI-108). The orange-shaded region indicates the reduced wavelength range accessible with the BSI-104. **b** Filtered spectra using the full (pink) and restricted (orange) interrogation windows. **c** Evolution of the SPR minimum with refractive index (RI) for the full (pink) and restricted (orange) spectra as well as results from BSI-104 interrogation. **d** Wavelength of the spectral local minimum as a function of interrogation window width. The orange and pink curves correspond to the full and restricted cases, respectively, while the light blue curve shows this minimum wavelength as the window narrows. **e** Spectrum measured with the BSI-104 interrogator. **f** Resulting spectra after applying the filtering-based method on (**e**).

incorporating Fourier-based signal processing with zero-padding, thereby mitigating the limitations imposed by the interrogator's spectral resolution. This allows the retrieval of robust sensing information from the cladding mode spectrum within a narrow spectral window, using instruments with sampling intervals as coarse as ~180 pm. This departs fundamentally from conventional interrogation techniques that rely on finely resolved tracking of individual resonances, often requiring expensive and bulky equipment.

The proposed approach reduces both hardware complexity and computational burden while preserving sensitivity and selectivity, even in non-ideal experimental conditions. We validate its performance in controlled refractometric environments as well as in clinically relevant biosensing scenarios. Importantly, the method remains resilient to spectral range truncation, provided the surface plasmon resonance dip is adequately captured. Moreover, we show that temperature-induced shifts can be compensated without referencing the Bragg mode, by tracking a dedicated cladding mode resonance within the same window. This reinforces the self-sufficiency of the system and simplifies the overall architecture.

Our results indicate that a lower-resolution system, while underestimating the absolute magnitude of spectral shifts by ~13%, preserves the fidelity of relative measurements. This precision proves sufficient for discriminating biological samples with distinct molecular signatures. In contexts where qualitative or threshold-based decisions are adequate, such as early-stage diagnostics or portable environmental monitoring, this level of performance is not only acceptable but desirable when balanced against cost, portability, and ease of use.

By reframing the interrogation process around the information content of the spectrum rather than its absolute resolution, this work addresses key limitations hindering the deployment of high-performance plasmonic sensors beyond laboratory settings. It opens the door to a new class of compact and cost-effective fiber optic biosensors, capable of delivering high-quality measurements with minimal infrastructure and accessible data processing, thereby advancing the integration of plasmonic fiber sensing into real-world biomedical and industrial applications.

Methods

Sensor fabrication

The fabrication process of Au-TFBGs, which serves as the basis for the biosensors used in this study, involves several steps. A silica telecommunication grade optical fiber (Corning SMF-28) is first hydrogen

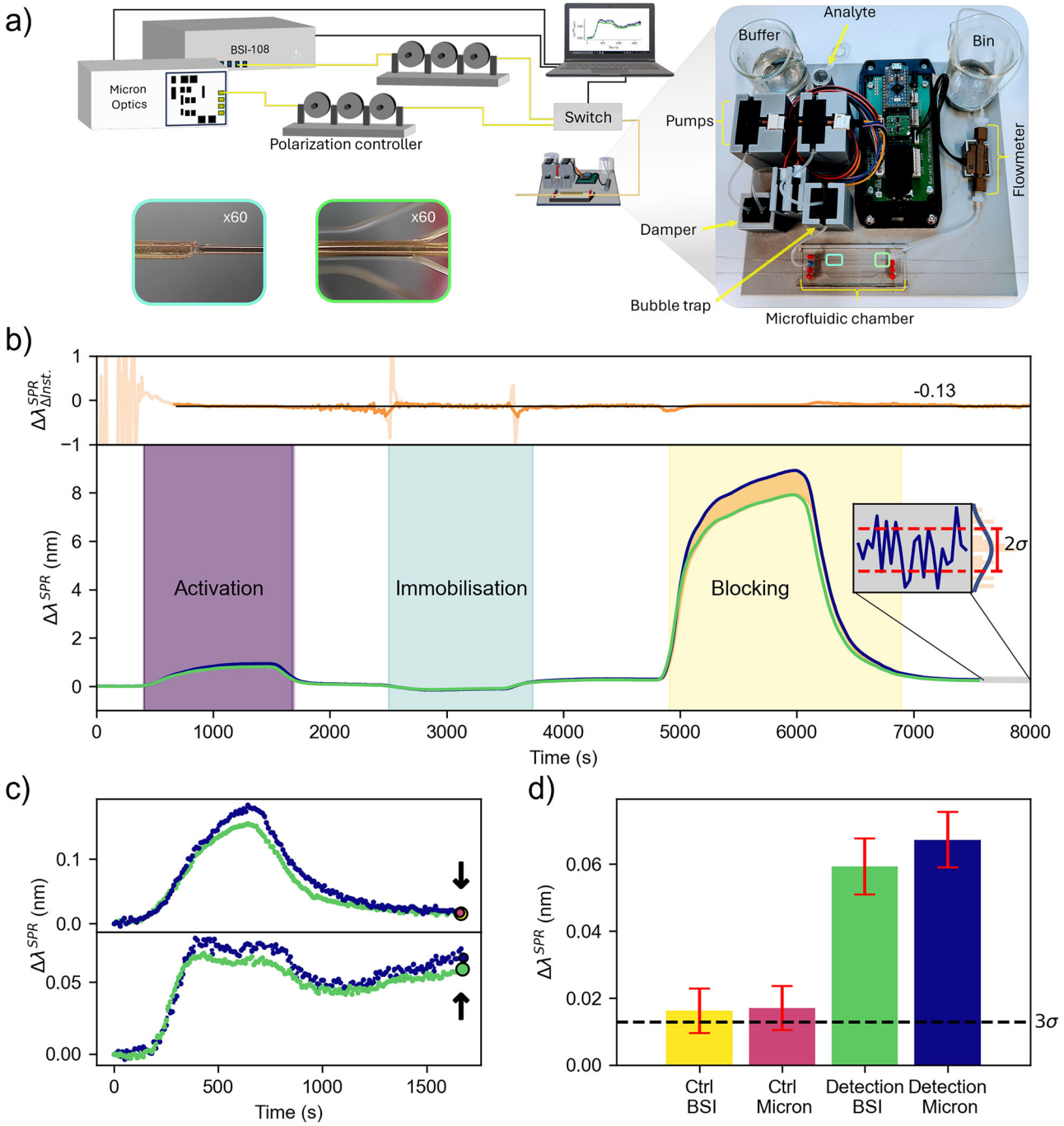

Fig. 5 | Biosensing with a gold-coated tilted fiber Bragg gratings (SPR-TFBG) using low- and high-resolution interrogators. a Experimental setup for microfluidic biosensing. **b** Surface functionalization steps monitored with both systems. **c** Spectral response to serum samples. Top panel: Control (Ctrl) solution, curves in blue and green matching the colors in (**b**). Bottom panel: PR3-positive serum, curves in blue and green. Black arrows indicate the last measurement, pointing to colored markers that highlight the measurement positions. Marker colors in the top panel are yellow and pink; in the bottom panel, blue and green. The arrows serve to guide the eye to the markers, which may partially overlap. **d** Differences in spectral shifts for control (Ctrl) and PR3-positive serum samples. Error bars correspond to ±1.96σ, where σ is the standard deviation of the baseline sensor response measured in buffer prior to analyte exposure.

loaded at ~200 bar and 60 °C for 30 h to enhance its photosensitivity. Then, using the phase mask technique, a tilted Bragg grating is inscribed within the fiber core. An excimer laser (Noria, from Northlab Photonics) operating at 193 nm is used in conjunction with an 7 or 8°-tilted phase mask with a period of 1100 nm. To remove excess hydrogen, the fiber is heated at 100 °C for 24 h. Finally, a 50 nm thick gold layer is deposited on the fiber using a sputter-coater Spuco equipped with 2" magnetron modules operating at a 250 W RF power supply. The deposition process is monitored using an inbuilt quartz microbalance with a resolution of 0.1 nm.

Interrogation device

Three FBG interrogators were employed to acquire the data presented in this study. The first system comprised a National Instruments PXIe-1071 chassis equipped with a PXIe-8135 embedded controller and a PXIe-4844 optical sensor interrogator. This setup offers a wavelength interrogation range from 1510.000 nm to 1589.996 nm with a sampling step of 4 pm, facilitating high-resolution spectral measurements.

The other two systems were BSI-104 and BSI-108 interrogators (BSENS, Belgium), both utilizing the DenseLight DL-US55016D-FS

superluminescent diode (SLED) as a broadband light source. The BSI-104 covers an interrogation range from 1525.151 nm to 1569.7584 nm, while the BSI-108 covers the range from 1508.5330 nm up to 1596.2739 nm. Both systems have a sampling interval of ~180 pm.

Experimental setup for temperature and RI characterization

The experimental setup, sketched in Fig. 2a, consists of two interrogators used to monitor a single SPR-TFBG. The sensor is connected to both instruments via a 1 × 4 optical switch (used as a 1 × 2 one), enabling sequential acquisition every 5 s. A polarization controller is placed upstream of the switch to optimize the input state of polarization and ensure the excitation of the SPR-attenuated ILs. The SPR-TFBG is immersed in a beaker filled with pure water initially heated to 50 °C using an AREX Digital stirrer-heater system from VELP Scientifica. Temperature monitoring is performed with an N-type thermocouple connected to a USB-TC-108 data logger from Pico Technology, enabling accurate tracking of the passive cooling process. For temperature measurements, a reference FBG, written in an SMF-28 fiber with a uniform grating period of 544 nm, was connected to the Micron Optics interrogator.

Experimental setup for biosensing

For the biosensing part, the Au-TFBG sensor is placed within a microfluidic chamber with a cross-section of $3.2 \pm 0.7\,mm^2$. The chamber, from microfluidic ChipShop GmbH, has a volume of 120 µL and features two inlets and one outlet, allowing for the alternating delivery of different solutions into the chamber. The output flow rate is regulated at 30 $\mu L\,min^{-1}$ to maintain a consistent flow rate during the experiments. The solutions are controlled using double diaphragm pumps integrated with a bubble trap and a pulsation damper (Micropumps mp6, mp-bt, and mp-damper from Bartel Mikrotechnik).

Reporting summary

Further information on research design is available in the Nature Portfolio Reporting Summary linked to this article.

Data availability

All data that support this study are available from the corresponding author upon reasonable request.

Code availability

Code to replicate this research can be requested from the corresponding author upon reasonable request.

Received: 1 June 2025; Accepted: 13 October 2025;
Published online: 24 November 2025

References

1. Kabashin, A. V. et al. Plasmonic nanorod metamaterials for biosensing. *Nat. Mater.* **8**, 867–871 (2009).
2. Damborsky`, P., Švitel, J. & Katrlík, J. Optical biosensors. *Essays Biochem.* **60**, 91–100 (2016).
3. Singh, P. SPR biosensors: historical perspectives and current challenges. *Sens. Actuators B Chem.* **229**, 110–130 (2016).
4. Liu, Y. et al. Surface plasmon resonance biosensor based on smart phone platforms. *Sci. Rep.* **5**, 12864 (2015).
5. Monk, D. J. & Walt, D. R. Optical fiber-based biosensors. *Anal. Bioanal. Chem.* **379**, 931–945 (2004).
6. Wang, W. et al. A label-free fiber optic SPR biosensor for specific detection of C-reactive protein. *Sci. Rep.* **7**, 16904 (2017).
7. Chen, C. & Wang, J. Optical biosensors: an exhaustive and comprehensive review. *Analyst* **145**, 1605–1628 (2020).
8. Mitu, S. A., Aktar, M. N., Ibrahim, S. M. & Ahmed, K. Surface plasmon resonance–based refractive index biosensor: an external sensing approach. *Plasmonics* **17**, 1581–1592 (2022).
9. Duan, Y. et al. TFBG-SPR DNA-biosensor for renewable ultra-trace detection of mercury ions. *J. Lightwave Technol.* **39**, 3903–3910 (2021).
10. Marquez-Cruz, V. & Albert, J. High resolution NIR TFBG-assisted biochemical sensors. *J. Lightwave Technol.* **33**, 3363–3373 (2015).
11. Prabhakar, A. et al. Evaluation of comparative sensitivity of embedded inner and outer bend surfaces of U-shaped waveguide for biochemical sensing application. *Microchem. J.* **208**, 112508 (2025).
12. Rajamani, A. S., Manoharan, H., Danny, C. G., Kishore, P. & Sai, V. Step-etched U-bent silica fiber optic probes–design and optimum geometry for refractive index sensing. *Sens. Actuators A Phys.* **342**, 113615 (2022).
13. Kelly-Richard, A. & Albert, J. Multiresonant analysis improves the limit of detection of tilted fiber Bragg grating refractometers. *Opt. Lett.* **47**, 3740–3743 (2022).
14. Fasseaux, H., Caucheteur, C. & Loyez, M. Unraveling plasmonic tilted fiber Bragg gratings (TFBG): a journey from “anomalous resonances” to refined refractometry. *Laser Photonics Rev.* **19**, 2400833 (2025).
15. Fasseaux, H., Loyez, M. & Caucheteur, C. Machine learning unveils surface refractive index dynamics in comb-like plasmonic optical fiber biosensors. *Commun. Eng.* **3**, 34 (2024).
16. Chubchev, E. D., Tomyshev, K. A., Nechepurenko, I. A., Dorofeenko, A. V. & Butov, O. V. Machine learning approach to data processing of TFBG-assisted SPR sensors. *J. Lightwave Technol.* **40**, 3046–3054 (2022).
17. Bashkatov, A. N. & Genina, E. A. Water refractive index in dependence on temperature and wavelength: a simple approximation. In *Saratov Fall Meeting 2002 Optical Technologies in Biophysics and Medicine IV*, vol. 5068, 393–395 (SPIE, 2003).
18. Raether, H. Surface plasmons on smooth surfaces. In *Surface Plasmons on Smooth and Rough Surfaces and on Gratings* 4–39 (Springer, 2006).
19. Yakubovsky, D. I., Arsenin, A. V., Stebunov, Y. V., Fedyanin, D. Y. & Volkov, V. S. Optical constants and structural properties of thin gold films. *Opt. Express* **25**, 25574–25587 (2017).
20. Genevieve, M. et al. Biofunctionalization of gold nanoparticles and their spectral properties. *Microelectron. Eng.* **84**, 1710–1713 (2007).
21. Schönermarck, U., Lamprecht, P., Csernok, E. & Gross, W. Prevalence and spectrum of rheumatic diseases associated with proteinase 3-antineutrophil cytoplasmic antibodies (ANCA) and myeloperoxidase-ANCA. *Rheumatology* **40**, 178–184 (2001).
22. Csernok, E. & Moosig, F. Current and emerging techniques for ANCA detection in vasculitis. *Nat. Rev. Rheumatol.* **10**, 494–501 (2014).
23. Bossuyt, X. et al. Revised 2017 international consensus on testing of ANCAs in granulomatosis with polyangiitis and microscopic polyangiitis. *Nat. Rev. Rheumatol.* **13**, 683–692 (2017).
24. Guchelaar, N. A. et al. The value of anti-neutrophil cytoplasmic antibodies (ANCA) testing for the diagnosis of ANCA-associated vasculitis, a systematic review and meta-analysis. *Autoimmun. Rev.* **20**, 102716 (2021).

Acknowledgements

This work was financially supported by the Fonds de la Recherche Scientifique - F.R.S.- FNRS under Senior Research Associate Grant of Christophe Caucheteur and the postdoctoral research grant of Médéric Loyez (C.R.) and the PDR Mosaic.

Author contributions

H.F. initiated the project, conducted the experiments to collect the data sets, and conceived the analysis algorithm; M.L. designed the biosensing experiments and co-directed the study with C.C. All authors contributed to the analysis, discussion, and writing of the manuscript.

Competing interests

The authors declare no competing interests.

Additional information

Supplementary information The online version contains supplementary material available at https://doi.org/10.1038/s44172-025-00534-y.

Correspondence and requests for materials should be addressed to Hadrien Fasseaux.

Peer review information *Communications Engineering* thanks Yang Ran and the other, anonymous, reviewers for their contribution to the peer review of this work. Primary Handling Editors: [Wenjie Wang, Rosamund Daw]. Peer reviewer reports are available.